

Reynolds Stress and Turbulent Energy Production in a Tidal Channel

TOM P. RIPPETH, EIRWEN WILLIAMS, AND JOHN H. SIMPSON

School of Ocean Sciences, University of Wales Bangor, Menai Bridge, Anglesey, United Kingdom

(Manuscript received 22 March 2001, in final form 7 September 2001)

ABSTRACT

A high-frequency (1.2 MHz) acoustic Doppler current profiler (ADCP) moored on the seabed has been used to observe the mean and turbulent flow components in a narrow tidally energetic channel over six tidal cycles at neap and spring tides. The Reynolds stress has been estimated from the difference in variance between the along-beam velocities of opposing acoustic beams with a correction for the sampling scheme and bin size. Shear stress was found to vary regularly with the predominantly semidiurnal tidal flow with the stresses on the spring ebb flow (up to 4.5 Pa) being generally greater than on the flood flow (<2 Pa) when the currents are weaker. The vertical structure approximated to linear stress profiles decreasing from maximum values near the bed to almost zero stresses just below the surface. The variation in the bed stress was well represented by a quadratic drag law, based on the depth-mean current, with an estimated drag coefficient of $2.6 \pm 0.2 \times 10^{-3}$.

The production of turbulent kinetic energy (TKE) followed a regular cycle at the M_4 frequency with maximum values exceeding 1 W m^{-3} near the bed during ebb flow at spring tides and decreasing with height to $\sim 10^{-3} \text{ W m}^{-3}$ at 2 m below the surface. Production was generally lowest ($\sim 10^{-4} \text{ W m}^{-3}$) at low water slack, which was longer than high water slack, and is marked by a rapid transition from flood to ebb. During peak ebb and flood the vertical distribution of production and the eddy viscosity N_z are reasonably well described by a proposed model based on the law of the wall and a steady balance between the pressure gradient and a uniform shear stress gradient.

The stress values have been incorporated into a trial dynamical balance based on the vertically integrated linearized equation of motion along the channel. The pressure gradient term is determined by two tide gauges separated by 5 km in the along-channel direction. The stress variation is in the correct phase to match the combined slope and acceleration term but is only about 60% of the magnitude required for balance. It is suggested that this discrepancy may result from an overestimation of the local pressure gradient, which may vary significantly between the tide gauges due to changes in the channel cross section.

1. Introduction

An understanding of turbulence is a key goal of shelf sea physical oceanography since turbulent processes are crucial in controlling flow dynamics and the vertical exchange of momentum and scalars within the water column. Until recently our knowledge of turbulence in shelf seas and estuaries has been severely limited by the difficulties of making measurements of the fluctuating velocity components in the interior of the water column remote from the fixed reference of the boundary. Studies of the turbulent velocities and shear stresses in the immediate bottom boundary layer advanced substantially following the pioneering measurements from bottom mounted tripods by Bowden and his coworkers (e.g., Bowden and Fairbairn 1956; Heathershaw 1979), but comparable midwater measurements to determine, for example, the components of the turbulent energy are

only now becoming possible with recent advances in technology.

The development of free-fall profilers for the measurement of finescale velocity shear has facilitated the observation of the rate of dissipation of the turbulent kinetic energy (Dewey et al. 1987; Simpson et al. 1996). Gargett (1994) developed an alternative method of estimating dissipation from measurements of larger-scale turbulent structures using an ADCP with one beam orientated to the vertical. Tropea (1981) proposed the use of a one-component laser Doppler anemometer for the direct estimation of the Reynolds stress and Lohrmann et al. (1990) extended this technique to the remote estimation of Reynolds stress profiles using an ADCP. This method, which relies on comparing velocity variances of opposing beams, is known as the "variance" method and has been employed in a number of shelf and estuarine studies of the evolution of the structure of turbulence (van Haren et al. 1994; Stacey et al. 1999a,b; Lu and Lueck 1999; Lu et al. 2000). The method also provides an estimate of the turbulent kinetic energy (TKE) and of the rate of production of TKE.

In this paper we report a series of new measurements

Corresponding author address: Tom Rippeth, School of Ocean Sciences, University of Wales Bangor, Menai Bridge, Anglesey, LL59 5EY, United Kingdom.
E-mail: t.p.rippeth@bangor.ac.uk

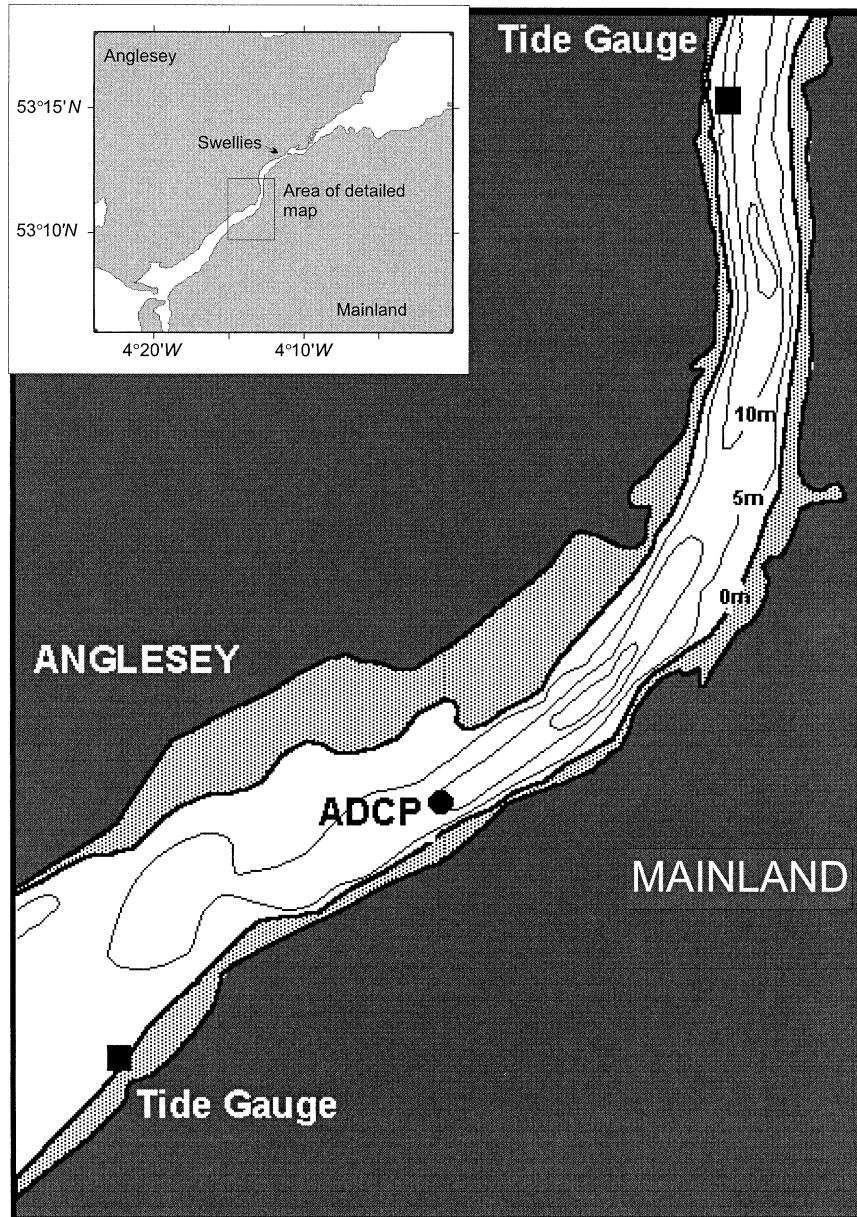


FIG. 1. The Menai Strait, with the insert showing the location and the main map the topography at the observational site. The topography is shown by depth contours 0 m (corresponding to lowest astronomical tide), 5 m, 10 m and 15 m. Gray indicates the area that dries out at low water. The symbols indicate the positions of the ADCP (solid circles) and the tide gauges (solid squares), A and B.

of the profile of stress and TKE production by the variance method in a well-mixed tidal channel using a bottom-mounted high-frequency (1.2 MHz) ADCP. The stress results are evaluated by comparison with the quadratic drag law and used in combination with the velocity shear to determine the TKE production and the eddy viscosity. We have also combined the stress results with measurements of the along-channel pressure gradient in a test of the first-order dynamical balance of the tidal flow in the strait.

2. Location and observational methods

a. The channel

Our observations were made in a central, sheltered section of Menai Strait (Fig. 1), a tidally energetic channel, which has a length of ~ 20 km and connects Caernarfon Bay to the northern Irish Sea. The channel has a mean width of approximately 800 m, narrowing to 300 m in an area known as the Swellies. In the wider sections of the strait there are large areas of sand banks

that are exposed at low water and lie on both sides of the main channel. The water depth in the main channel at low water of a spring tide varies from only a few meters (in the Swellies) to a maximum of 22 m.

The strait is subjected to strong tidal currents, reaching speeds of up to 2.5 m s^{-1} at a spring tide in the Swellies and at the southwest entrance. When the tide is towards the northeast, the sea level is rising for most of the time, so this period is referred to as the flood (and defined as the positive x direction for the purposes of this paper). When the flow is directed to the southwest it is termed ebb (negative x direction). The flow is asymmetric with larger currents occurring on the ebb than on the flood and particularly large accelerations apparent in the transition from the flood to ebb. Rectification of the tidal flow by nonlinear effects, mainly in the shallow Swellies region, produces a net residual flow to the southwest ranging from $800 \text{ m}^3 \text{ s}^{-1}$ at a spring tide to $330 \text{ m}^3 \text{ s}^{-1}$ at neaps (Simpson et al. 1971). The strength of the tidal currents ensures that the water column is almost always well mixed in the vertical. Freshwater input into the channel is small and along-channel density gradients are generally weak (Campbell et al. 1998). The section of the strait chosen for the experiment is sheltered and so rarely experiences surface waves of amplitude $>0.5 \text{ m}$.

b. Experimental setup

An RDI 1.2-MHz Workhorse ADCP was deployed on the seabed in midchannel (Fig. 1) for a spring tide period (30 June–3 July 2000) and a neap tide period (10–13 July 2000). A third, shorter deployment to cover a single tidal cycle was made in October 2000. The site of the deployment was in mean water depth of 15 m close to the location used in previous studies (Campbell et al. 1998). The channel width here varies between 900 m at high water and 500 m at low water. The ADCP was deployed in a purpose-built heavy frame; in situ pitch and roll measurements indicate the vertical axis of the instrument was $< 2^\circ$ from the vertical in all cases. Lu and Lueck (1999) show that the maximum error in the stress estimate from a 2° tilt is $< 17\%$.

In each case the ADCP was set up to record the along-beam velocities with a ping rate of 2 Hz. For both spring and neap deployments the bin size was set to 0.5 m and the data were ensemble-averaged over 2 seconds (i.e., 4 pings). For the third, single tidal cycle deployment, the instrument was set up to record every individual ping, and the bin size was reduced to 25 cm. In all cases the ADCP was deployed in the standard RDI mode 1 in which the noise characteristics can be assumed to be independent of the velocities measured (RDI 2000). With the ambiguity velocity set to 1.7 m s^{-1} , the standard deviation of the uncertainty associated with each horizontal velocity estimate was 0.033 m s^{-1} for the spring and neap deployments and 0.12 m s^{-1} for the single tidal cycle deployment.

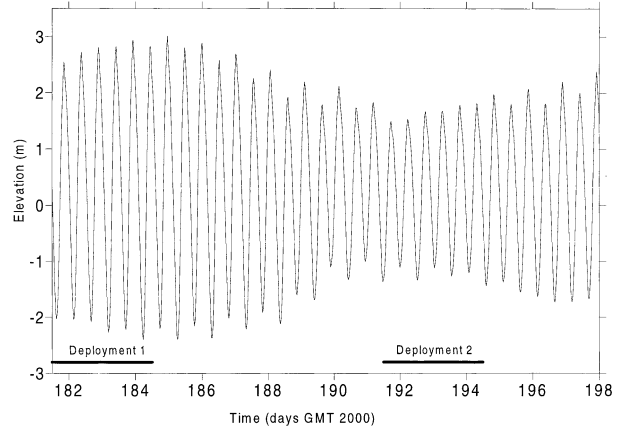


FIG. 2. Sea surface elevation from tide gauge B showing the timing of the spring (deployment 1) and neap (deployment 2) measurements.

The timing of the spring and neap deployments in relation to the cycle of tidal elevation is shown in Fig. 2. In order to determine the along-channel pressure gradient, two tide gauges were deployed at positions (Fig. 1) separated by a distance of $\sim 5 \text{ km}$ along the axis of the channel. The tide gauges were fixed at a level close to the lowest astronomical tide and leveled in to bench marks before and after the deployment. Both instruments logged data continuously for a 4-week period covering both the spring and neap ADCP deployments. The sea surface height above the seabed at the ADCP position was estimated independently using the ADCP backscatter measurements following the method of Visbeck and Fischer (1995).

3. Data analysis

The along-beam velocities (b_i , where $i = 1, 4$) were separated into a mean over 10 min, \bar{b}_i , and fluctuating quantity, b'_i , as

$$b_i = \bar{b}_i + b'_i.$$

The Reynolds stress estimates were calculated using the variance technique proposed by Lohrmann et al. (1990) and described in detail by Stacey et al. (1999a), in which

$$\begin{aligned} \frac{\tau_x}{\rho} &= \overline{u'w'} = \frac{\text{var}(b_3) - \text{var}(b_4)}{2 \sin 2\theta}; \\ \frac{\tau_y}{\rho} &= \overline{v'w'} = \frac{\text{var}(b_1) - \text{var}(b_2)}{2 \sin 2\theta}, \end{aligned} \quad (1)$$

where $\text{var}(\)$ indicates the variance of a quantity and θ is the angle each beam makes with the vertical (20° for the instrument used). The axes are chosen so that the opposing beams 3 and 4 lie in the x - z plane and so determine τ_x , while beams 1 and 2 lie in the y - z plane and provide the estimate of τ_y . In the subsequent analysis we rotated the coordinates to give the axial (x) and cross-channel (y) components of stress.

The estimation of turbulent parameters requires that the velocity field can be assumed to be horizontally homogeneous so that the statistics of the turbulence are the same for each of the four beams (Lu and Lueck 1999). An assumption of stationarity is also necessary and this imposes constraints on the length of record we can use in the analysis. The averaging period must be of sufficient duration to provide a good sample of the largest turbulent eddies, but not so long that the turbulent processes cannot be regarded as quasi stationary. In the present case, where our time series are dominated by variability at the semidiurnal frequency, a reasonable compromise between statistical reliability and stationarity is an initial sample length of 10 min.

Our sampling strategy, which is based on a compromise between temporal resolution and record duration, involves the averaging of four pings at 0.5-s intervals to give estimates of the along-beam velocity. Typically, the autocorrelation function of the fluctuating velocities falls to less than 0.5 in a time of ~ 4 s, which means that there will be a significant loss of variance, and thus underestimation of the Reynolds stress, when we calculate the 4-ping average. In addition there may be some apparent loss of stress due to the bin size being comparable in scale to some of the smaller eddies that are involved in momentum transfer in the vertical.

We have used the data from the single tidal cycle deployment, in which every ping was recorded and a bin size of 25 cm was used, to investigate these effects on stress estimates. The Reynolds stresses from the single-ping deployment were initially calculated using every ping and a 10-min averaging period (1200 pings). Then, in order to replicate the ADCP internal averaging procedure used in the spring and neap deployments, a 2-s, 4-ping mean velocity was calculated by averaging velocity estimates from adjacent depth bins and groups of 4 pings. A second estimate of the Reynolds stress was then obtained using the new velocity estimate. A comparison of the along-channel stress estimated from single-ping data from a 25-cm bin with the estimate made using the 4-ping mean data and a 50-cm bin size is given in Fig. 3. Regression analysis of the ~ 12 h of data indicates that the stresses from the 4-ping data are underestimated by $\sim 23\%$ relative to the single-ping results. We have therefore applied a correction of 1.30 to all our stress estimates. Most of this correction is attributable to the 4-ping averaging with only a relatively small contribution ($\sim 20\%$ of the total) from the effect of the bin size. We assume in the subsequent analysis that this correction factor is constant and can be applied to all our data.

4. Results

a. The Reynolds stress

To give a general impression of the cycle of stress variation over a semidiurnal cycle, we show, in Fig. 4a, vertical profiles of the Reynolds stress acting in the

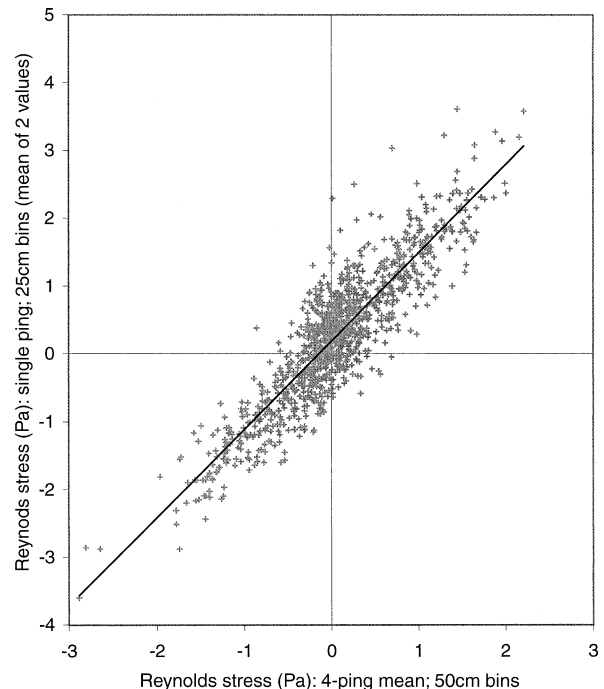


FIG. 3. (a) Comparison of the along-stream Reynolds stress (Pa) calculated using single-ping data from 25-cm bins and from 4-ping averaged data for 50-cm bins for the single tidal cycle deployment. The fit has an $r^2 = 0.80$ with 1080 degrees of freedom and gives a gradient of 1.30.

along-channel (x) direction for each hour of one tidal cycle together with the corresponding current profiles (Fig. 4b). The stresses generally decrease more or less linearly from extreme values near the seabed (1.5 mab) to negligible values at the highest level observed (~ 1 m below the surface). A possible exception to the linear trend in the observed stress gradients occurs at peak ebb flow during the spring deployment when the stress was observed to significantly decrease in the last few bins above the instrument on three tidal cycles out of six. Around slack water the stresses throughout the water column are close to zero. The largest stress magnitudes occur at times of highest flow speeds with considerable asymmetry between the ebb and flood. During the ebb, near-bed stress exceeds 3 Pa at the time of maximum depth mean flow speed (~ 1.2 m s^{-1}) while during the flood stresses are limited to ~ -2 Pa during the peak flood, depth-mean, flow of ~ 0.95 m s^{-1} .

This asymmetry is clearly evident in a contour plot (fig. 5), which shows the stress variation over the full neap deployment of six tidal cycles. The stress cycle is seen to be highly regular and dominated by the along-channel component while the cross-channel stress τ_y rarely exceeds a magnitude of 0.5 Pa. Another aspect of asymmetry in the stress is evident in the behavior at successive slack waters. Around low water slack, the period of low stress (< 0.5 Pa) lasts ~ 2 h compared to ~ 1 h around high water slack when there is a rapid

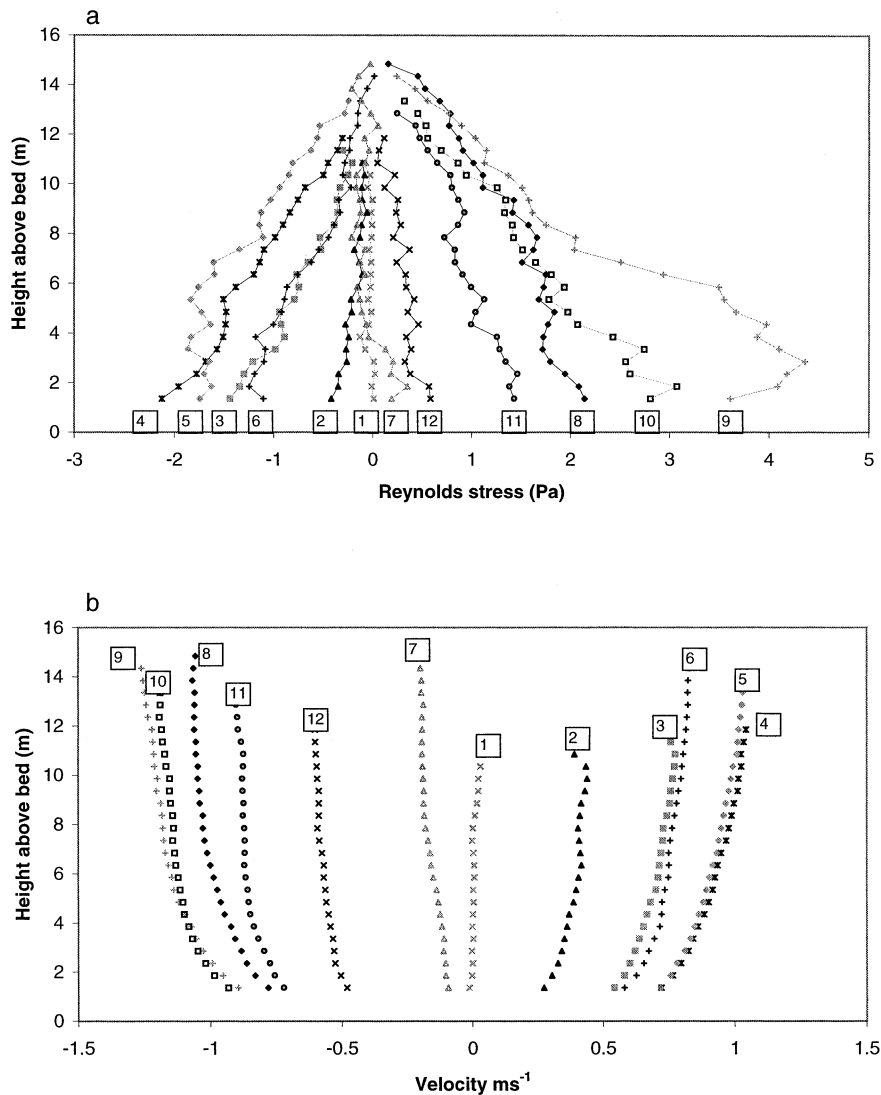


FIG. 4. Stress and velocity profiles over a single tidal cycle during the spring deployment. The boxed numbers indicate the sequence of the hourly measurements: (a) Reynolds stress (Pa) profiles averaged over each hour of the tidal cycle. (b) Mean velocity (m s^{-1}) profiles at times corresponding to stress profiles in (a).

switch from flood to ebb commencing before local high-water and leading to peak ebb flow occurring just after high water.

In Fig. 6 we have compared the along-channel bed stress τ_b , extrapolated from the lowest bin with the quadratic drag law by plotting against $\rho|U|U$ where U is the depth-averaged current. Both neap and spring data show a satisfactory fit ($r^2 > 0.93$ with 425 degrees of freedom) to a straight line with compatible slopes, which yield a mean drag coefficient of $C_d = 2.6 \times 10^{-3}$ with an uncertainty ($2 \times$ standard error) of $\pm 0.2 \times 10^{-3}$.

A further check on the stress estimate can, in principle, be made by determining u_* from the mean velocity profile via a logarithmic fit. Here u_* values were estimated in this way for the lowest seven bins of the

alongstream mean velocity profile, and those values that were deemed a good fit (i.e., $r^2 > 0.95$) were then compared to values calculated by linear extrapolation of the stress estimate for the closest ADCP bin to the seabed assuming zero stress at the surface. Table 1 shows the ratio of the u_* estimated from the stress method to the value estimated by a log fit. This ratio is calculated for both spring and neap deployments and subdivided between the flood and ebb phases of the tide. In each case the ratio is significantly less than 1 (note that in each case the standard error < 0.025) but the standard deviation values (σ) indicate a large spread in the data. The ratio shows that the ebb values are larger than the flood values, and are only slightly less than unity in the neap case.

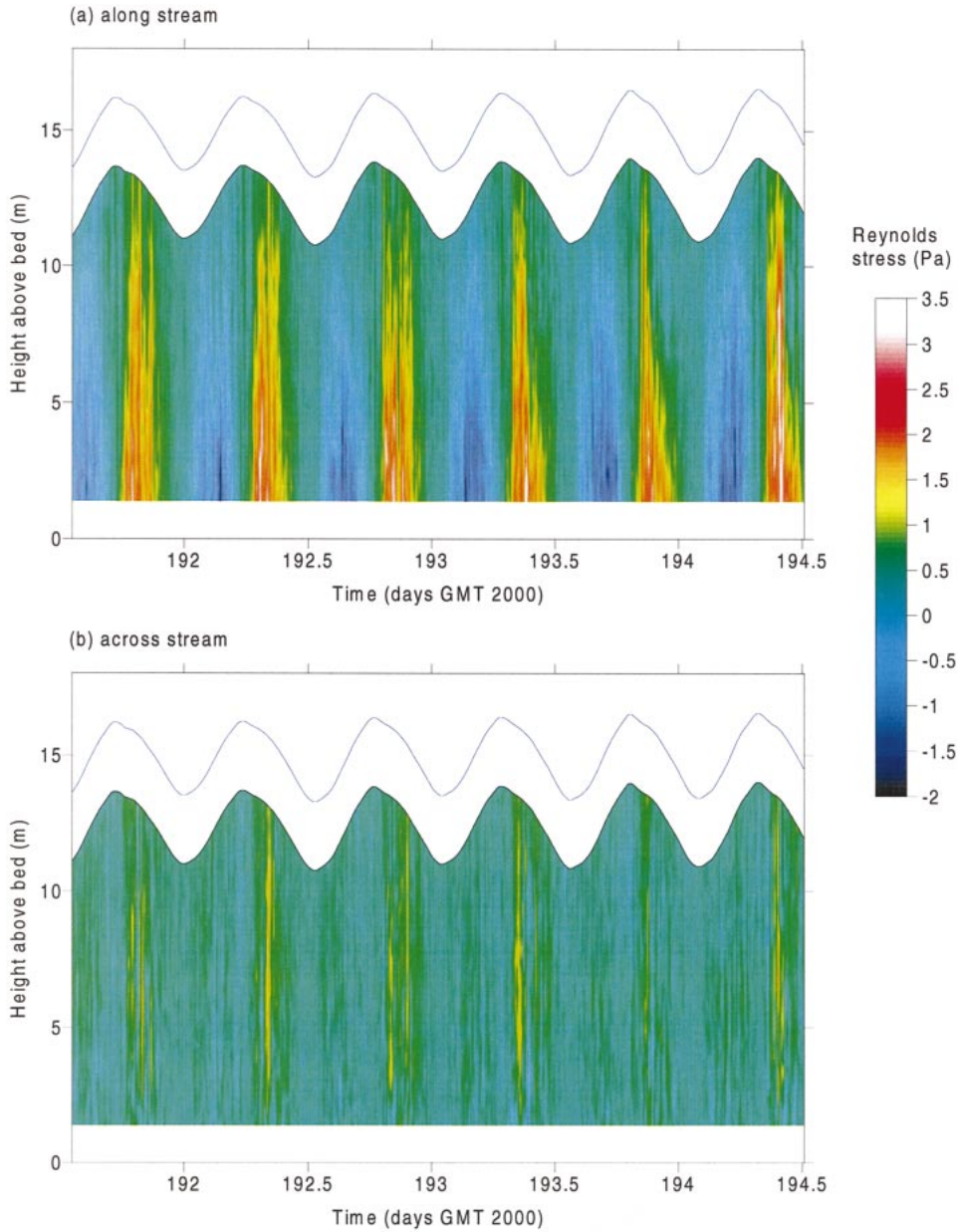


FIG. 5. Reynolds stress (Pa) for the neap deployment (a) along channel and (b) across channel.

A cause for concern over the log profile method is that, if we extend the fit to include higher levels, the apparent stress increases, although the goodness of fit remains high and this introduces a degree of arbitrariness into the method.

b. TKE production

The rate P at which energy is transferred from the mean flow to turbulent kinetic energy is estimated from the product of the Reynolds stress and the velocity shear according to

$$P = -\tau_x \frac{\partial \bar{u}}{\partial z} - \tau_y \frac{\partial \bar{v}}{\partial z} = -\rho \left(\overline{u'w'} \frac{\partial \bar{u}}{\partial z} + \overline{v'w'} \frac{\partial \bar{v}}{\partial z} \right). \quad (2)$$

A contoured plot of P during the springs and neap deployments (Fig. 7) shows the highest rate of production is consistently found near the seabed with levels decreasing by about two orders of magnitude between the lowest and highest bins. Near the bed (1.5 mab) at peak ebb flow on springs, the maximum P exceeds 1 W m^{-3} while lowest values occur at low water slack when production falls to $\sim 10^{-4} \text{ W m}^{-3}$. The rate of production of TKE is related to the speed of the current and exhibits

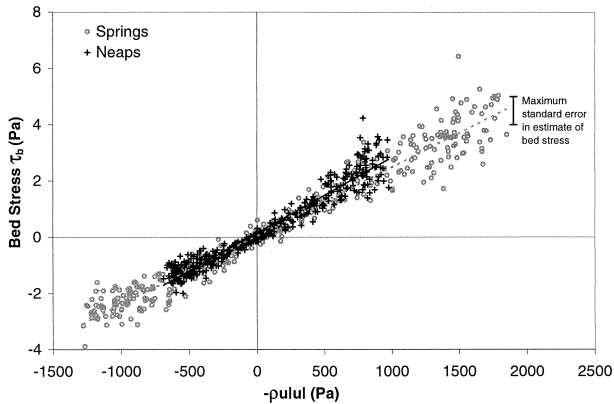


FIG. 6. Comparison of the Reynolds stress estimates with the quadratic drag law bed stress (Pa) is plotted vs $\rho|U|U$ where U is the depth-mean current for (a) spring and (b) neap deployments. Both fits have $r^2 > 0.93$ and 425 degrees of freedom.

a dominant quarter-diurnal variation throughout the water column with the exception of the uppermost part of the water column where, during neap, the M_4 response is muted. As with the stress, P is not symmetric between flood and ebb; for both deployments, the peak flood value just above the bed is typically 60% of that observed at maximum ebb.

We have compared the rate of production P at peak flow, when the acceleration is near zero, with a model based on the law of the wall, which gives the velocity shear in the axial direction as $\partial u/\partial z = u_*/\kappa z$, where z is the height above the bed, u_* is the friction velocity, and $\kappa = 0.41$ is von Kármán's constant. We assume further that there is a steady balance between the pressure gradient and frictional stress during peak flow so that the shear stress varies linearly with height from its value at the bed $\tau_b = -\rho u_*^2$, to zero at the surface, a supposition justified by the observations. Under these conditions, the rate of TKE production at a specific height would be given by

$$P = -\tau \frac{\partial u}{\partial z} = -\tau_b \left(1 - \frac{z}{h}\right) \frac{u_*}{\kappa z} = \frac{\rho u_*^3}{\kappa} \left(\frac{1}{z} - \frac{1}{h}\right). \quad (3)$$

Plots of the observed TKE production versus z at peak ebb and flood are shown in Fig. 8a together with P from the steady flow model [Eq. (3)] with a value of u_* determined from a regression fit of production to $1/z$. There is generally satisfactory agreement between the two for both ebb and flood profiles, but on the flood there is a slight but consistent deviation from the theory for levels above $z = 10$ mab where values are significantly lower than the law of the wall model.

According to this same model, the eddy viscosity should be given by

$$N_z = \frac{-\tau}{\rho(\partial u/\partial z)} = \frac{-\tau_b(1 - z/h)}{(u_*/\kappa z)} = \kappa u_* z \left(1 - \frac{z}{h}\right). \quad (4)$$

We have compared N_z inferred from the observed stress

TABLE 1. The mean ratio of u_* estimates using the stress methods and u_* estimated using the log-profile method.

| Deployment | Spring | Spring | Neap | Neap |
|-------------|--------|--------|-------|-------|
| Tidal phase | Flood | Ebb | Flood | Ebb |
| Mean ratio | 0.763 | 0.870 | 0.813 | 0.955 |
| σ | 0.143 | 0.182 | 0.185 | 0.239 |

and mean shear with the predictions of Eq. (4). Although there is considerable scatter in the N_z values, the profiles, when averaged over 60 min (Fig. 8b), are consistent with the parabolic form given in Eq. (4). The values of u_* agree well with those estimated directly from the stress and through a log fit to the velocity profile, except for those estimated to fit the N_z profile on the ebb tide, which are substantially larger than those estimated by other methods.

A partial explanation of the considerable scatter in N_z relative to the model, and the overestimate in u_* using this model, is that the estimates of shear in the upper part of the water column during the ebb are very small (Fig. 9), and so is likely to be subject to relatively large errors.

5. Dynamical balance

As a further test of the validity of our stress measurements we have used the stress results together with surface slope estimates from the tide gauge data to construct a trial dynamic balance following the approach of Campbell et al. (1998). We use a linearized form of the along-channel dynamical equation

$$\frac{\partial U}{\partial t} + g \frac{\partial \eta}{\partial x} = -\frac{\tau_b}{\rho h}, \quad (5)$$

where $\partial U/\partial t$ is the depth-averaged flow acceleration obtained from the ADCP. The pressure gradient term $-g\partial\eta/\partial x$ is approximated by the difference between the tide gauge levels divided by their separation along the channel (~ 5 km), while the mean stress divergence $\tau_b/(\rho h)$ is found from the stress at the lowest bin divided by the height of the water column above it. A small correction ($\sim 3\%$) has been applied for the effects of transverse slope induced by the earth's rotation since the two tide gauges were on opposite sides of the channel.

In Fig. 10 we have plotted the stress divergence term against the sum of the acceleration and slope terms [lhs of Eq. (5)] and included data for both spring and neap deployments. The data conform reasonably well to straight-line fits with well-determined slopes that are closely similar for the two cases. The measured stress is therefore varying in the right phase to match the other forces but the magnitude of the regression slope (the mean gradient = 0.59 ± 0.02) is significantly less than the unity value that would denote dynamical balance.

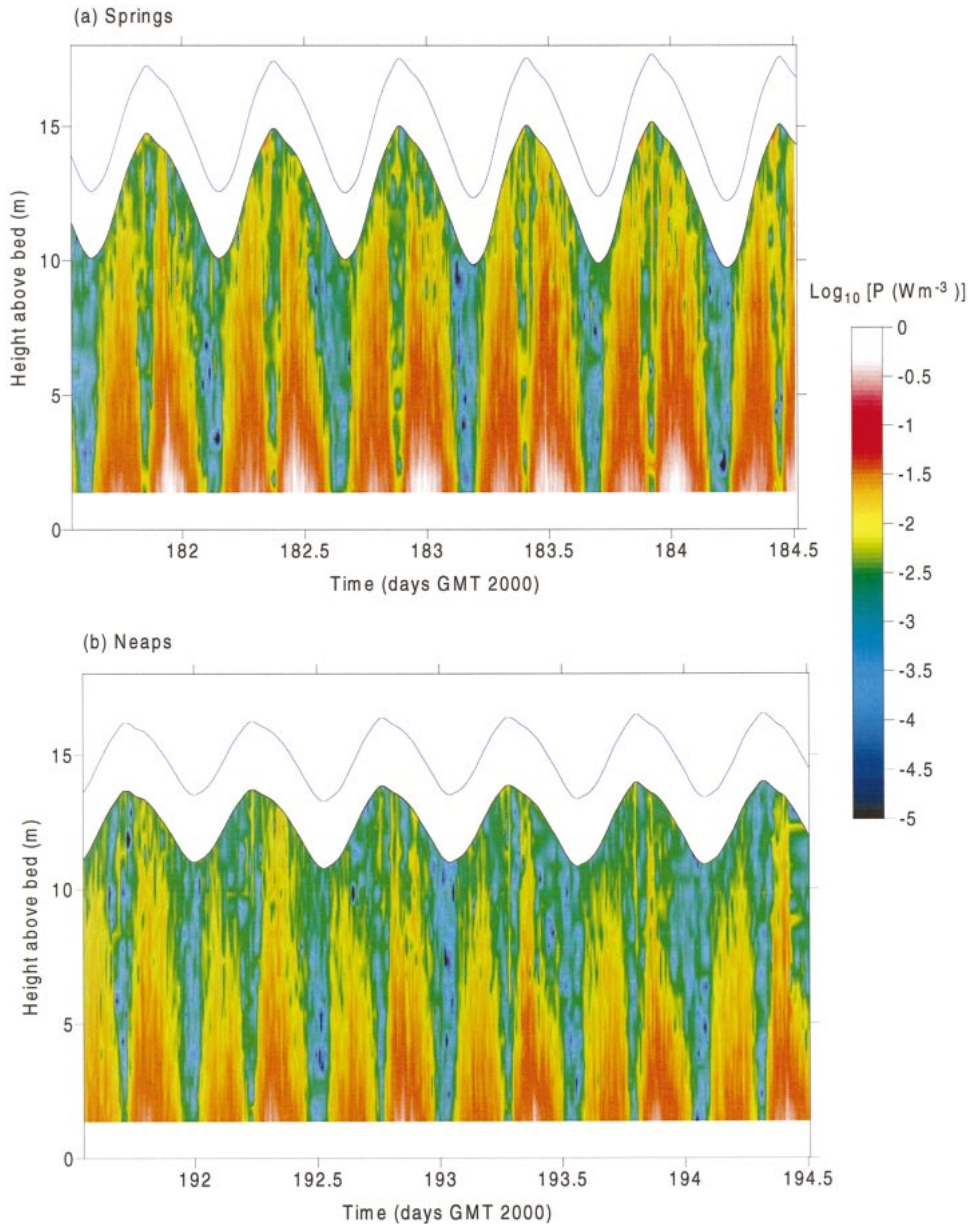


FIG. 7. Rate of production of turbulent kinetic energy (W m^{-3}) for the deployments at (a) spring and (b) neap.

6. Summary and discussion

The present study advances the approach of Stacey et al. (1999a) and Lu et al. (2000) by utilizing high quality data from a bottom-mounted high-frequency ADCP to provide stress profiles over several tidal cycles. A correction for the effect of averaging over multiple pings and finite bin size has been identified and the correction factor determined by a short time series of single-ping data. The corrected stress results have been combined with velocity shear to yield new estimates of the vertical structure of TKE production and the eddy viscosity. Around maximum flow, both of these

parameters are found to accord reasonably well with a proposed model based on a pressure gradient versus friction balance with the shear according to the law of the wall. Further confidence has been given to the variance method by comparing the values extrapolated to the bed with the quadratic drag law. We have further proposed a new test that involves the construction of a dynamical balance over the tidal cycle using measured values of the surface slope and the acceleration terms.

The stress values show a good fit to the quadratic drag law with consistent slopes on the neap and spring deployments. The drag coefficient, based on the depth-

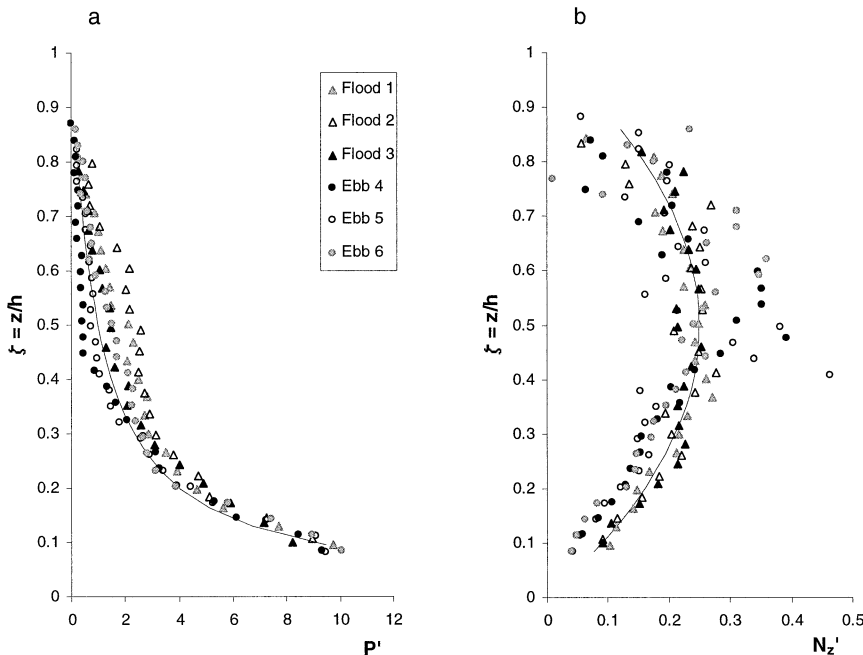


FIG. 8. (a) Nondimensionalized production profiles, P' (where $P' = P\kappa h/\rho u_*^3$), at peak flood (solid triangles) and ebb (solid circles) flow compared with the steady-flow model (solid line). (b): Profiles of nondimensionalized eddy viscosity, N'_z (where $N'_z = N_z/\kappa u_* h$), at peak flood (solid triangles) and ebb (solid circles) flow compared with the steady-flow model (solid line).

mean flow, is found to be $C_d = 2.6 \pm 0.2 \times 10^{-3}$. The stress falls off more or less uniformly with height above the bed, decreasing to near zero at the surface. TKE production, which depends on the product of stress and velocity gradient, decays rapidly with distance from the bottom boundary and, to a first approximation, follows a model based on the law of the wall and a uniform stress gradient. The eddy viscosity N_z inferred from the

stress and velocity is also well-determined and the profiles at peak flow exhibit parabolic profiles that are consistent with this same model.

There remains the question of the incomplete dynamical balance. In principle, this could be due either to a further underestimation of the stress or to overestimation of the other terms in the dynamical equation. The correction for 4-ping averaging of the variances, which we have applied (section 3), was based on a linear regression fit of the single-ping data for the stresses on the stress based on 4-ping averages. It is arguable that, since

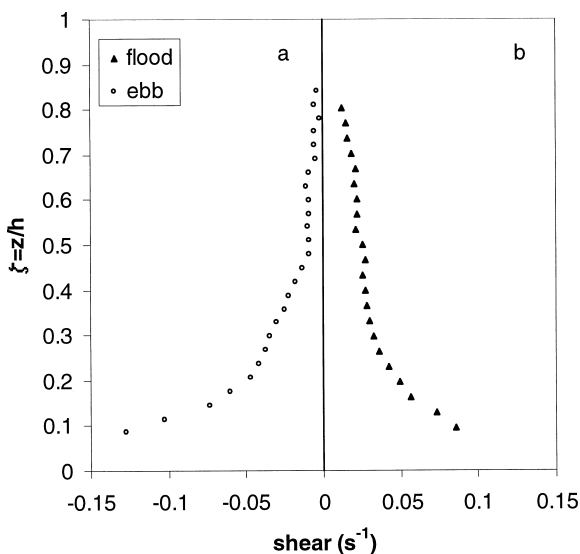


FIG. 9. Typical profiles of the mean velocity shear taken during periods of peak ebb and peak flood flow.

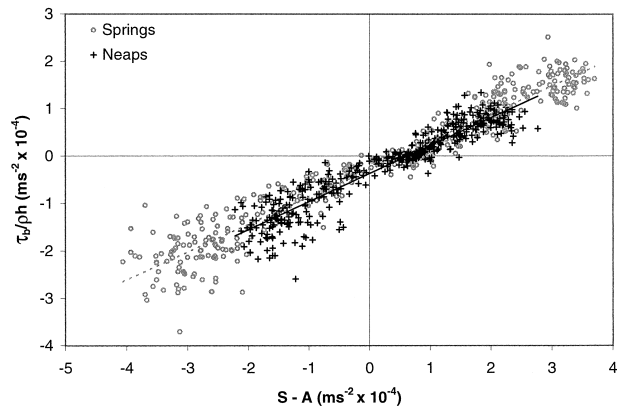


FIG. 10. Trial dynamical balance. The stress divergence $\tau_b/(\rho h)$ is plotted against the combined slope and acceleration terms ($S-A$). The regression line for the combined dataset from neaps and springs has a slope of 0.61 indicating incomplete balance.

both these quantities are subject to random errors, a neutral regression (Garrett and Petrie 1981) should be used. This procedure gives a correction factor of 1.45 as against 1.30, which would increase our estimates of the stress by $\sim 11\%$, which is still insufficient to account for the dynamical imbalance. There are also doubts about the validity of the neutral regression approach (Emery and Thompson 1998). More likely, the discrepancy arises from uncertainties in the determination of the leading pressure gradient term, which is based on the difference between elevation measured by two tide gauges 5 km apart. The difference yields an estimate of the mean slope along this section of the channel, which for a uniform channel would approximate closely to the local gradient. For our channel, however, there are significant variations in depth, breadth, and form of the channel that we estimate could lead to differences between the mean and local gradient of up to $\approx 30\%$.

The comparison of u_* estimated from the stress profiles and from the mean velocity profile via a logarithmic fit shows that, despite a large scatter in the values, the estimate from the mean velocity profiles is consistently larger than the estimate from the stress profile. Lu et al. (2000) report a similar result but with a larger discrepancy, even when the 4-ping to single-ping correction is implemented, with a ratio of ~ 0.73 . They suggest that the difference between the two methods arise from the fact that the variance method measures only the skin frictional drag of the bottom while the log profile also incorporates contributions due to larger-scale form drag. An alternative explanation for the differences reported here is the advection of turbulence along the channel, which may make a different contribution on the ebb and the flood and result in the observed asymmetry in the flow.

Finally it is perhaps worth noting that the strategy of averaging several pings and then correcting for the stress reduction due to ensemble averaging offers significant advantages in allowing extended data recording. This procedure does, however, require a determination of the correction factor, which may vary between turbulent regimes. In the long term a preferable solution will be the in situ processing of the ping data so that only the stress and mean flow parameters need to be stored.

Acknowledgments. Alan Nield and Gwyn Parry Jones provided invaluable technical support. TPR is in receipt

of a Natural Environmental Research Council Research Fellowship and EW is in receipt of a NERC studentship.

REFERENCES

- Bowden, K. F., and L. A. Fairbairn, 1956: Measurements of turbulent fluctuations and Reynolds stresses in a tidal current. *Proc. Roy. Soc. London*, **A237**, 422–438.
- Campbell, A. R., J. H. Simpson, and G. L. Allen, 1998: The dynamical balance of flow in the Menai Strait. *Estuarine, Coastal Shelf Sci.*, **46**, 449–455.
- Dewey, R. K., W. R. Crawford, A. E. Gargett, and N. S. Oakey, 1987: A microstructure instrument for profiling oceanic turbulence in coastal bottom boundary layers. *J. Atmos. Oceanic Technol.*, **4**, 288–297.
- Emery, W. J., and R. E. Thomson, 1998: *Data Analysis Methods in Physical Oceanography*. Pergamon Elsevier Science, 634 pp.
- Gargett, A. E., 1994: Observing turbulence with a modified acoustic doppler current profiler. *J. Atmos. Oceanic Technol.*, **11**, 1592–1610.
- Garrett, C., and B. Petrie, 1981: Dynamical aspects of the flow through the Strait of Belle Isle. *J. Phys. Oceanogr.*, **11**, 376–393.
- Heathershaw, A. E., 1979: The turbulent structure of the bottom boundary layer in a tidal channel. *Geophys. J. Roy. Soc.*, **58**, 395–430.
- Lohrmann, A., B. Hackett, and L. P. Røed, 1990: High resolution measurements of turbulence, velocity and stress using a pulse-to-pulse coherent sonar. *J. Atmos. Oceanic Technol.*, **7**, 19–37.
- Lu, Y., and R. G. Lueck, 1999: Using a broadband ADCP in a tidal channel. Part II: Turbulence. *J. Atmos. Oceanic Technol.*, **16**, 1568–1579.
- , —, and D. Huang, 2000: Turbulence characteristics in a tidal channel. *J. Phys. Oceanogr.*, **30**, 855–867.
- RDI, 2000: Application note FSA-003—Broadband ADCP water profiling modes. RDI, 6 pp.
- Simpson, J. H., A. M. G. Forbes, and W. J. Gould, 1971: Electromagnetic observations of water flow in the Menai Strait. *Geophys. J. Roy. Astron. Soc.*, **24**, 245–253.
- , W. R. Crawford, T. P. Rippeth, A. R. Campbell, and J. V. S. Cheok, 1996: The vertical structure of turbulent dissipation in shelf seas. *J. Phys. Oceanogr.*, **26**, 1579–1590.
- Stacey, M. T., S. G. Monismith, and J. R. Burau, 1999a: Measurements of Reynolds stress profiles in unstratified tidal flow. *J. Geophys. Res.*, **104**, 10 933–10 949.
- , —, and —, 1999b: Observations of turbulence in a partially stratified estuary. *J. Phys. Oceanogr.*, **29**, 1950–1970.
- Tropea, C., 1981: A note concerning the use of a one-component LDA to measure shear stress terms. *Exp. Fluids*, **1**, 209–210.
- van Haren, H., N. Oakey, and C. Garrett, 1994: Measurements of internal wave band eddy fluxes above a sloping bottom. *J. Mar. Res.*, **52**, 909–946.
- Visbeck, M., and J. Fischer, 1995: Sea surface conditions remotely sensed by upward-looking ADCPs. *J. Atmos. Oceanic Technol.*, **12**, 141–149.